Nuclear Science and Techniques (2025) 36:215
https://doi.org/10.1007/s41365-025-01792-3

Continuous Bayesian probability estimator in predictions of nuclear charge radii

Jian Liu[1] · Kai-Zhong Tan[1] · Lei Wang[2] · Wan-Qing Gao[1] · Tian-Shuai Shang[3] · Jian Li[3] · Chang Xu[4]

Received: 9 January 2025 / Revised: 21 February 2025 / Accepted: 14 March 2025 / Published online: 30 August 2025

Abstract

Recently, machine learning has become a powerful tool for predicting nuclear charge radius R_C, providing novel insights into complex physical phenomena. This study employs a continuous Bayesian probability (CBP) estimator and Bayesian model averaging (BMA) to optimize the predictions of R_C from sophisticated theoretical models. The CBP estimator treats the residual between the theoretical and experimental values of R_C as a continuous variable and derives its posterior probability density function (PDF) from Bayesian theory. The BMA method assigns weights to models based on their predictive performance for benchmark nuclei, thereby accounting for the unique strengths of each model. In global optimization, the CBP estimator improved the predictive accuracy of the three theoretical models by approximately 60%. The extrapolation analyses consistently achieved an improvement rate of approximately 45%, demonstrating the robustness of the CBP estimator. Furthermore, the combination of the CBP and BMA methods reduces the standard deviation to below 0.02 fm, effectively reproducing the pronounced shell effects on R_C of the Ca and Sr isotope chains. The studies in this paper propose an efficient method to accurately describe R_C of unknown nuclei, with potential applications in research on other nuclear properties.

Keywords Machine learning · Nuclear charge radii · Continuous Bayesian probability estimator · Bayesian model averaging

1 Introduction

The nuclear charge radius R_C is a fundamental property of atomic nuclei and plays a crucial role in research on nuclear structures [1]. It provides insights into various phenomena, including shape coexistence [2], neutron skin [3–5], proton halo [6], shell structure [7], odd–even staggering [8, 9], and nuclear matter saturation [10]. There are two main experimental methods for measuring R_C. One directly determines R_C through experiments such as muonic atom X-ray spectroscopy (μ^-) [11] and high-energy elastic electron scattering (e^-) [12, 13]. The second type analyzes subtle differences between isotopes to indirectly measure R_C, for instance, K_α X-ray isotope shifts (K_αIS) [14] and optical isotope shifts (OIS) [15]. Recently, advancements in laser spectroscopy techniques have enabled precise determination of R_C for over 130 unstable nuclei [16–21]. Nevertheless, challenges in the experimental measurement of R_C persist, especially in the production of exotic isotopes and in improving experimental sensitivity, making it difficult to understand nuclear structures in unexplored regions.

Many theoretical models have been developed to study R_C, from macroscopic formulas to sophisticated microscopic approaches. First, a conventional approach to estimate R_C is a semi-empirical formula based on the $A^{1/3}$ law or the $Z^{1/3}$ dependence of the liquid drop model, improved

This work was supported by the National Natural Science Foundation of China (Nos. 12475135, 12035011, and 12475119), the Shandong Provincial Natural Science Foundation, China (No. ZR2020MA096), and the Fundamental Research Funds for the Central Universities (No. 22CX03017A).

✉ Jian Liu
liujian@upc.edu.cn

[1] College of Science, China University of Petroleum (East China), Qingdao 266580, China

[2] School of Physics Science and Engineering, Tongji University, Shanghai 200092, China

[3] College of Physics, Jilin University, Changchun 130012, China

[4] Department of Physics, Nanjing University, Nanjing 210093, China

by introducing effects such as shell structure, isospin, and odd–even nuclear effects [22–24]. Subsequently, local-relation-based models determine R_C from the properties of neighboring nuclei [25–28], with prominent examples being the Garvey–Kelson relation [29, 30] and mirror nuclei relation [31, 32]. Additionally, more sophisticated mean-field nuclear structure models offer self-consistent descriptions of R_C and other nuclear properties. Examples include the Skyrme–Hartree–Fock–Bogoliubov (HFB) models [33–36], relativistic mean-field (RMF) models [37–41], and relativistic Hartree–Bogoliubov (RHB) models [42–44]. Recent studies in Refs. [45, 46] have systematically calculated properties such as nuclear binding energy, charge radii, and electric quadrupole moment based on the deformed RHB theory in continuum. Finally, a class of *ab initio* approaches, such as the no-core shell model (NCSM), starts from realistic nucleon interactions and provides a precise description of R_C by solving the many-body Schrödinger equation or the corresponding self-consistent field equations [47, 48]. Theoretical models have achieved significant advancements, reducing root-mean-square errors to below 0.05 fm and providing satisfactory descriptions of the unique behaviors of R_C in isotope chains. However, as the accuracy requirements for calculations increase, the complexity of theoretical models also increases significantly.

In recent years, machine learning (ML) techniques have been widely applied in nuclear physics [49, 50], including nuclear mass studies [51–59], charge density distributions [60, 61], nuclear decay [62–66], and nuclear reactions [67–69], particularly for predicting R_C [70–75]. Initially, the ML method was applied to train the experimental values of R_C, independent of the theoretical models. As early as 2013, researchers have utilized artificial neural networks (ANN) to predict R_C by directly generating a formula [70]. Subsequently, to incorporate the strengths of the theoretical models, ML techniques were employed to refine them by estimating the residuals between the theoretical and experimental values of R_C. Early work in 2016 proposed a Bayesian neural network (BNN) with a single hidden layer to optimize these predictions [71]. Later, multiple research groups significantly enhanced the robustness of BNN by introducing physical effects and adding input features [72–74]. Notably, the naive Bayesian probability (NBP) classifier, which applies Bayesian theory and *k-means* clustering, reframes the prediction of R_C as a classification task. This approach demonstrated strong extrapolation capabilities and provided uncertainty in prediction [75, 76].

Recently, the application of the continuous Bayesian probability (CBP) estimator and the Bayesian model averaging (BMA) further improved the reliability of nuclear mass descriptions [77]. Unlike the NBP method, which discretizes the residuals δ of the theoretical model, the CBP estimator considers δ as a continuous variables. By combining the Bayesian framework with kernel density estimation (KDE), the CBP estimator derives a posterior probability density function (PDF) of δ for the target nuclei. This method demonstrates a robust predictive performance and can explain intrinsic numerical relationships. Moreover, the BMA method combines the predictive strengths of different theoretical models across distinct regions of the nuclear chart, further improving overall performance [78–80].

This study combines the CBP estimator and BMA method to optimize the predictions of R_C. The initial theoretical values of R_C were calculated separately using the HFB, RHB, and semi-empirical liquid drop models. First, the global optimization capability of the CBP estimator was evaluated by comparing its predictions with experimental data from the 2013 compilation of nuclear charge radii [16]. Subsequently, its extrapolation capability was investigated using the learning set from the 2004 compilation [11] to predict R_C for nuclei newly reported in the 2013 compilation. After optimization using the CBP estimator, to further improve the predictive accuracy for nuclei near the drip line, the BMA method was applied to assign weights to each model based on their predictive performance on the benchmark nuclei. The benchmark nuclei selected in this study are ^{49}K [81], ^{38}Ca [82], ^{100}Cd, ^{119}Cd [83], ^{201}Po [84], and ^{233}Ra [85]. Finally, we predict R_C of the Ca and Sr isotopic chains using the CBP estimator in combination with the BMA method to verify the ability of this approach to capture the physical effects on R_C. The approaches proposed in this study can be used to investigate R_C of unknown nuclei, with potential applications in the study of other nuclear properties.

This paper is structured in three sections: Sect. 2 introduces the theoretical framework of the CBP and BMA methods. Section 3 presents the results of these methods. Section 4 provides the summary of this study.

2 Theoretical framework

The theoretical framework offers detailed procedures and formulas for a continuous Bayesian probability (CBP) estimator and the Bayesian model averaging (BMA). A method for evaluating the predictive performance and a formula for quantifying the uncertainties are also presented.

2.1 The continuous Bayesian probability method

In the CBP estimators, the residuals δ of R_C are treated as continuous variables and their posterior PDFs are derived from Bayesian theory. The estimated residuals, which are used to correct the theoretical models, can then be calculated from the posterior PDFs.

For continuous multivariate variables, given a set of features or variables $X_1, X_2, \ldots, X_m$ and a target variable Y, the posterior PDF can be expressed as

$$p(Y|X) = \frac{p(X_1|Y)p(X_2|Y)\cdots p(X_m|Y)p(Y)}{\int p(X_1|Y)p(X_2|Y)\cdots p(X_m|Y)p(Y)\mathrm{d}Y}. \quad (1)$$

The conditional PDF $p(X_i|Y)$ represents the likelihood of observing events X_i given the occurrence of Y, whereas the prior PDF $p(Y)$ denotes the frequency of occurrence for a given Y. The denominator in Eq. (1) acts as a normalization constant, ensuring that the posterior PDF $p(Y|X)$ is integrated to unity.

According to Eq. (1), event Y represents the continuous residual δ. Events X_i correspond to the proton number Z_t and neutron number N_t of the target nucleus. It is assumed that Z_t and N_t are independent of other variables. Thus, the posterior PDF can be expressed as

$$p(\delta|Z_\mathrm{t}, N_\mathrm{t}) = \frac{p(Z_\mathrm{t}|\delta)p(N_\mathrm{t}|\delta)p(\delta)}{\int p(Z_\mathrm{t}|\delta)p(N_\mathrm{t}|\delta)p(\delta)\mathrm{d}\delta}. \quad (2)$$

The conditional PDFs $p(Z_\mathrm{t}|\delta)$ and $p(N_\mathrm{t}|\delta)$ in Eq. (2) can be derived using the following univariate Bayesian formula,

$$p(Z_\mathrm{t}|\delta) = \frac{p(\delta|Z_\mathrm{t})p(Z_\mathrm{t})}{p(\delta)}, \quad (3)$$

$$p(N_\mathrm{t}|\delta) = \frac{p(\delta|N_t)p(N_t)}{p(\delta)}. \quad (4)$$

In Eqs. (3) and (4), the prior probability $p(Z_\mathrm{t}(N_\mathrm{t}))$ was calculated from the occurrence frequencies of $Z_\mathrm{t}(N_\mathrm{t})$ in the learning set. The likelihood PDFs $p(\delta|Z_\mathrm{t})$ and $p(\delta|N_\mathrm{t})$ are estimated using kernel density estimation (KDE).

$$p(\delta|Z_\mathrm{t}) = \frac{1}{n_Z h_Z}\sum_{i=1}^{n_Z} K\left(\frac{\delta-\delta_i}{h_Z}\right), \quad (5)$$

$$p(\delta|N_\mathrm{t}) = \frac{1}{n_N h_N}\sum_{i=1}^{n_N} K\left(\frac{\delta-\delta_i}{h_N}\right), \quad (6)$$

where $h_{Z(N)}$ denotes the bandwidth parameter and $n_{Z(N)}$ represents the number of nuclei in the learning set that have the same $Z_\mathrm{t}(N_\mathrm{t})$ as the target nucleus. Kernel function $K(t)$ is specified as a Gaussian kernel because the residuals follow a Gaussian distribution:

$$K(t) = \frac{1}{\sqrt{2\pi}}\mathrm{e}^{-\frac{t^2}{2}}. \quad (7)$$

Similarly, the prior PDF $p(\delta)$ can also be obtained using KDE,

$$p(\delta) = \frac{1}{nh_\delta}\sum_{i=1}^{n} K\left(\frac{\delta-\delta_i}{h_\delta}\right), \quad (8)$$

where h_δ denotes the bandwidth parameter, and n is the total number of nuclei in the learning set. In Eqs. (5), (6), and (8), the individual residual δ_i is defined as $\delta_i = R^{\mathrm{exp}}_{\mathrm{C},i} - R^{\mathrm{th}}_{\mathrm{C},i}$. The values chosen for the bandwidth parameters h_δ, h_Z, and h_N depend on several factors, including the range of δ_i, the size of the dataset, and the level of noise in the data.

When determining the likelihood PDF and prior PDF, a weight function is introduced to account for the local relationship between neighboring nuclei:

$$w(Z,N;Z_\mathrm{t},N_\mathrm{t}) = \exp\left[-\frac{(Z-Z_\mathrm{t})^2+(N-N_\mathrm{t})^2}{\rho}\right]+\varepsilon. \quad (9)$$

Parameter ρ significantly affects the prediction performance and extrapolation range of the CBP estimator. Based on the distribution characteristics of the nuclei from the dataset on the nuclear chart, $\rho = 4$ was selected for this study. Parameter ε affects the stability of the posterior PDF, and $\varepsilon = 10^{-10}$ was chosen to ensure a Gaussian distribution for $p(\delta|Z_\mathrm{t},N_\mathrm{t})$. The prior PDF and likelihood PDF with the applied weights are as follows:

$$p_{\mathrm{wt}}(\delta) = \frac{1}{nh_\delta}\sum_{i=1}^{n} K\left(\frac{\delta-\delta_i}{h_\delta}\right)w(Z_i,N_i;Z_\mathrm{t},N_\mathrm{t}), \quad (10)$$

$$p_{\mathrm{wt}}(\delta|Z_\mathrm{t}) = \frac{1}{n_Z h_Z}\sum_{i=1}^{n_Z} K\left(\frac{\delta-\delta_i}{h_Z}\right)w(Z_i,N_i;Z_\mathrm{t},N_\mathrm{t}), \quad (11)$$

$$p_{\mathrm{wt}}(\delta|N_\mathrm{t}) = \frac{1}{n_N h_N}\sum_{i=1}^{n_N} K\left(\frac{\delta-\delta_i}{h_N}\right)w(Z_i,N_i;Z_\mathrm{t},N_\mathrm{t}). \quad (12)$$

The posterior PDF $p(\delta|Z_\mathrm{t},N_\mathrm{t})$ is obtained by combining Eqs. (2)–(12), and the expected value was used to determine the estimated residual of the target nucleus.

$$\delta^{\mathrm{em}}(Z,N) = \int \delta p(\delta|Z,N)\mathrm{d}\delta. \quad (13)$$

Ultimately, the refined nuclear charge radius is obtained by appending the estimated residual $\delta^{\mathrm{em}}(Z,N)$ to the theoretical nuclear charge radius $R^{\mathrm{th}}(Z,N)$:

$$R^{\mathrm{corr}}_{\mathrm{C}}(Z,N) = R^{\mathrm{th}}_{\mathrm{C}}(Z,N) + \delta^{\mathrm{em}}(Z,N). \quad (14)$$

2.2 Bayesian model averaging

Even after refinement by the CBP estimator, individual models often fail to comprehensively account for all physical phenomena, owing to their varying strengths and weaknesses in

different regions of the nuclear chart. To consider the advantages of different models in the isotopic and isotonic chains, Bayesian model averaging (BMA) was introduced [86].

The BMA method is based on the Bayesian theorem and assigns weights to each model by assessing its predictive performance. Specifically, given a set of K candidate models $M_1, \ldots, M_K$, the BMA method calculates posterior probabilities based on the predictions for the benchmark nucleus from each model. These posterior probabilities serve as the weights for each model and are calculated as follows:

$$P(M_k|D) = \frac{P(D|M_k)P(M_k)}{\sum_{i=1}^{K} P(D|M_i)P(M_i)}. \tag{15}$$

In this study, the six selected benchmark nuclei in dataset D were ^{49}K, ^{38}Ca, ^{100}Cd, ^{119}Cd, ^{201}Po, and ^{233}Ra, which were used to evaluate the accuracy of the models based on the entire nuclide chart. Residuals were obtained using three theoretical models: the HFB model with SLy4 parameterization, RHB model with PK1 parameter set, and semi-empirical liquid drop model. The prior probability $P(M_k) = 1/K$ is related to the number of candidate models, and the conditional probability $P(D|M_k)$ depends on the predictive performance of each theoretical model,

$$P(D|M_k) = \prod_{j}^{J} \frac{1}{\sqrt{2\pi}\mu} \exp\left[-\frac{\left(\delta_{k,j}^{\mathrm{corr}}\right)^2}{2\mu^2}\right], \tag{16}$$

where J denotes the total number of benchmark nuclei. The refined residuals $\delta_{k,j}^{\mathrm{corr}}$ for the j-th benchmark nucleus corresponding to the theoretical model M_k are defined as $\delta_{k,j}^{\mathrm{corr}} = R_{k,j}^{\mathrm{exp}} - R_{k,j}^{\mathrm{corr}}$. The parameter μ is used to normalize the values of $\delta_{k,j}^{\mathrm{corr}}$ and is defined by

$$\mu = \sqrt{\frac{1}{K \cdot J} \sum_{k=1}^{K} \sum_{j=1}^{J} (\delta_{k,j}^{\mathrm{corr}})^2}. \tag{17}$$

Finally, the average nuclear charge radius calculated using the BMA method is:

$$\bar{R}(Z_{\mathrm{t}}, N_{\mathrm{t}}) = \sum_{i=1}^{K} R_{\mathrm{C},i}^{\mathrm{corr}} P(M_i|D). \tag{18}$$

The discrepancies between the corrected theoretical predictions and the experimental data for each model were assessed using the standard deviation σ_{rms}, defined as

$$\sigma_{\mathrm{rms}}^2 = \frac{1}{n} \sum_{i=1}^{n} \left(R_{\mathrm{C},i}^{\mathrm{exp}} - R_{\mathrm{C},i}^{\mathrm{corr}}\right)^2. \tag{19}$$

In the CBP estimator, the prediction uncertainties are obtained from the posterior PDF. The one-sigma uncertainty $\sigma^{\mathrm{em}}(Z,N)$ of each model corresponding to a specific nucleus (Z, N) is defined as

$$\sigma^{\mathrm{em}}(Z,N) = \sqrt{\int [\delta - \delta^{\mathrm{em}}(Z,N)]^2 p(\delta|Z,N)\mathrm{d}\delta}, \tag{20}$$

and the uncertainty of the BMA is given by

$$\sigma^{\mathrm{BMA}}(Z,N) = \sum_{i=1}^{K} \sigma_i^{\mathrm{em}} P(M_i|D). \tag{21}$$

3 Results

In this section, the theoretical values of R_{C} are initially calculated using the HFB model with SLy4 parameterization, RHB model with the PC-PK1 parameter set [87], and three-parameter semi-empirical formula of Sheng et al. [88]. Notably, the RHB model is based on the relativistic continuum Hartree–Bogoliubov theory and incorporates nucleon intrinsic electromagnetic structure corrections [89, 90]. Subsequently, the initial results were refined by employing the CBP estimator and BMA method. The entire set comprises 892 nuclei with proton numbers $Z > 3$ sourced from the 2013 charge radii compilation [16]. The global optimization and extrapolation capabilities of the CBP estimator are evaluated, followed by an analysis of the extrapolation performance of the approach that combines the CBP and BMA methods.

3.1 Global optimizations of the CBP estimator

The theoretical R_{C} values of 892 nuclei were calculated using three models, and the raw residuals $\delta^{\mathrm{pre}} = R_{\mathrm{C}}^{\mathrm{exp}} - R_{\mathrm{C}}^{\mathrm{th}}$ for each nucleus were obtained. Subsequently, the CBP estimator was applied to refine the predictions of each model. According to Sect. 2, the posterior PDF $p(\delta|Z_{\mathrm{t}}, N_{\mathrm{t}})$ of the target nucleus can be calculated by Eqs. (2)–(12). The refined charge radius $R_{\mathrm{C}}^{\mathrm{corr}}(Z_{\mathrm{t}}, N_{\mathrm{t}})$ was then obtained using Eqs. (13) and (14). The HFB and RHB models in this study were solved under the assumption of spherical symmetry. In the entire set, the majority of δ^{pre} is distributed within the range of −0.1 fm to 0.1 fm. For nuclei with identical proton or neutron numbers, the variation in δ^{pre} is typically limited to within 0.05 fm. Based on the distribution characteristics of δ^{pre}, the bandwidth parameters were selected as $h_\delta = 0.07$ fm, $h_Z = 0.01$ fm, and $h_N = 0.02$ fm. Table 1 presents the standard deviations σ_{pre} of the three theoretical models before optimization and σ_{post} after optimization by the CBP estimator. The global optimization performance of

Table 1 The standard deviation σ_{pre} (fm) from the theoretical models and σ_{post} (fm) after the CBP and NBP refinements. 892 nuclei in 2013 charge radii compilation with $Z > 3$ are chosen as the entire set

Methods		HFB	RHB	Sheng
CBP	σ_{pre}	0.040	0.047	0.042
	σ_{post}	0.016	0.017	0.016
	$\Delta\sigma/\sigma_{\text{pre}}$	60.0%	63.8%	61.9%
NBP	σ_{post}	0.020	0.021	0.023
	$\Delta\sigma/\sigma_{\text{pre}}$	50.0%	55.3%	45.2%

the CBP estimator was evaluated using the improvement rate $\Delta\sigma/\sigma_{\text{pre}} = (\sigma_{\text{pre}} - \sigma_{\text{post}})/\sigma_{\text{pre}}$.

As shown in Table 1, the standard deviations σ_{pre} for the spherical HFB, RHB, and semi-empirical formulas are approximately 0.04 fm. However, the deformed mean-field theories give a standard deviation of approximately 0.03 fm [41, 42]. After refining using the CBP estimator, the standard deviations σ_{post} for both spherical models are further reduced to approximately 0.016 fm, representing an improvement of approximately 60%. This improvement demonstrates the advantages of the CBP estimator. The CBP estimator can introduce deformation effects into the calculations of spherical theoretical models using statistics, thereby improving the description of R_{C} for deformed atomic nuclei.

To illustrate the progress achieved by the CBP method, Table 1 presents the optimization performance of the NBP method for comparison. The NBP method is a discrete Bayesian probabilistic approach that employs the *k-means* algorithm to determine the cluster centers δ_i, which are then used to refine the theoretical models. For the three models, the improvement rate of the CBP method is approximately 10% higher than that of the NBP method. This arises from the CBP estimator treating residuals as continuous variables and obtaining the estimated residual value δ^{em} by integrating the posterior PDF over the entire residual distribution, rather than using a discrete posterior probability, as in the NBP method. The CBP estimator accounts for all possible residual contributions, thereby achieving a higher degree of optimization and demonstrating a clear advantage.

To further illustrate the performance of the CBP estimator across the different models and regions, Fig. 1 presents the raw residuals (gray dots) from the HFB model, the RHB model, and the semi-empirical formula, along with the corrected residuals (blue dots) after applying the CBP estimator. It is evident that after CBP optimization, the residuals for all three theoretical models were remarkably reduced across most regions. This improvement can be attributed to the CBP estimator framework. Based on the global description of theoretical models, the CBP estimator utilizes a statistical approach to further capture the local correlation effects among nuclei with identical proton or neutron numbers. The

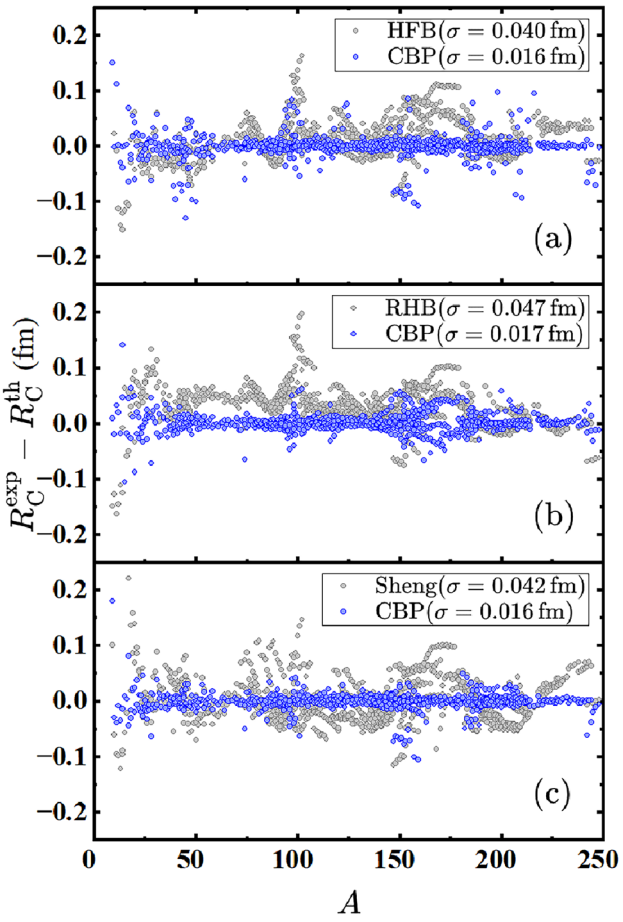

Fig. 1 The charge radii residuals $\delta = R_{\text{C}}^{\text{exp}} - R_{\text{C}}^{\text{th}}$ from the experimental data as a function of mass number A. The gray dots denote the raw results from the HFB calculations, and the blue dots denote the predicted residuals after the CBP refinements. **b** and **c** the same as **a**, but for the results from RHB model and Sheng's formula, respectively

introduction of the weight function ensures that only nuclei in close proximity to the target nucleus on the nuclear chart significantly influence the prediction, thereby enhancing the sensitivity of the CBP estimator to local correlation effects. Therefore, the CBP estimator is more effective in regions where local correlations are stronger, and the distribution of δ^{pre} is more regular, such as regions with pronounced shell effects.

In regions $60 < A < 90$, $120 < A < 140$, and $215 < A < 240$ in Fig. 1a; $45 < A < 90, 110 < A < 140$, and $220 < A < 240$ in Fig. 1b; and $80 < A < 95, 110 < A < 145$, and $210 < A < 240$ in Fig. 1c, where theoretical model predictions exhibit similar accuracy and the distribution of δ^{pre} is highly regular, the CBP estimator achieves substantial improvements, considerably reducing the residuals. In particular, for nuclei with mass numbers around $A = 100$, $A = 150$, and $A = 190$, where proton–neutron residual interactions and other physical effects lead to large δ^{pre}, the CBP

method markedly enhances the predictive accuracy by statistically accounting for these interactions and effects. However, for light nuclei, where δ^{pre} exhibits greater variability owing to relatively low nucleon numbers, the optimization effect of the CBP estimator is comparatively limited. As more charge radii of light nuclei are precisely measured in experiments, the predictive performance of the CBP estimator for light nuclei can be further enhanced.

3.2 Extrapolating capabilities of the CBP estimator

Model extrapolation was essential for the acquisition of unknown data. In this section, we evaluate the extrapolation performance of the CBP estimator. The learning set comprised 790 nuclei with proton numbers $Z > 3$ from the 2004 charge radii compilation [11], while the validation set included 102 experimental charge radii added between 2004 and 2013. The bandwidth parameters h_δ, h_N, and h_Z used in the extrapolation process are the same as those employed in the global optimization. The standard deviations σ_{pre} and σ_{post} for the learning and validation sets, both before and after applying the CBP estimator, are reported in Table 2 along with the optimization rate $\Delta\sigma/\sigma_{\text{pre}}$.

According to Table 2, the standard deviations of R_{C} calculated using the HFB, RHB, and semi-empirical formulas are approximately 0.040 fm for both the learning and validation sets. This consistency indicates that the initial theoretical models possess considerable extrapolation capabilities, which are more beneficial for the CBP estimator in predicting unknown regions. After applying the CBP estimator, the standard deviations for all three models in the learning set decreased to less than 0.020 fm, achieving an improvement of approximately 60% compared to the initial results. In the validation set, the standard deviations were slightly greater than 0.020 fm, with improvement rates of approximately 45% for the three models. The steady improvement rates across both the learning and validation sets demonstrate the robust extrapolation capabilities of the CBP estimator.

The optimization rates for all three models in the validation set were lower than those in the learning set. This phenomenon can be explained by the CBP framework: the Bayesian formula accounts for statistical correlations among nuclei with the same proton and neutron numbers, whereas the weight function considers local relationships among neighboring nuclei. Most nuclei in the validation set were positioned near the drip line, where fewer neighboring nuclei were represented in the learning set, thereby diminishing the performance of the CBP estimator. As more R_{C} values were measured experimentally, the extrapolation ability of the CBP estimator was expected to improve significantly.

The results in Table 2 indicate that the CBP estimator demonstrates excellent extrapolation capabilities. The HFB, RHB, and semi-empirical formulas provide the overall trends of R_{C} variations. By inheriting the advantages of theoretical models and incorporating local correlation characteristics between nuclei, the CBP estimator captures the physical effects that are not reflected in theoretical models, leading to reliable corrections of R_{C}. Consequently, for nuclei lacking experimental data, the CBP estimator can offer precise and robust predictions.

3.3 Comprehensively factoring in the results of different models using the BMA method

After optimization using the CBP estimator, specific models exhibited optimal predictive performance in distinct regions, especially for nuclei far from the β-stability line. This study introduces the BMA method to integrate these strengths. The BMA method assigns weights based on the predictive performance of different models for the benchmark nuclei. To balance the predictive discrepancies between the theoretical models across different regions of the nuclear chart, the benchmark nuclei selected for the BMA method were ^{49}K, ^{38}Ca, ^{100}Cd, ^{119}Cd, ^{201}Po, and ^{233}Ra, which cover a wide range of the nuclear chart, including from light nuclei to heavy nuclei and from proton-rich regions to neutron-rich regions. These selected nuclei are located near the edges of the nuclear chart and are outside the 2013 charge radii compilation, making them particularly valuable for benchmarking extrapolation capabilities.

After obtaining the corrected residuals $\delta^{\text{corr}} = R_{\text{C}}^{\text{exp}} - R_{\text{C}}^{\text{corr}}$ for the benchmark nuclei, the weights for each model were calculated using the BMA method and the results are presented in Table 3. The HFB model exhibits

Table 2 The raw standard deviation σ_{pre} (fm) from the theoretical models and the standard deviation σ_{post} (fm) after the CBP estimator refinements. The learning set includes 790 nuclei with $Z > 3$ in the 2004 compilation, and the validation set includes the newly added 102 nuclei in the 2013 compilation

Models	Learning set			Validation set		
	σ_{pre}	σ_{post}	$\Delta\sigma/\sigma_{\text{pre}}$	σ_{pre}	σ_{post}	$\Delta\sigma/\sigma_{\text{pre}}$
HFB	0.040	0.017	57.5%	0.038	0.021	44.7%
RHB	0.046	0.017	63.0%	0.052	0.025	51.9%
Sheng	0.042	0.018	57.1%	0.043	0.026	39.5%

Table 3 The corrected residuals $\delta^{\rm corr}$(fm) of six benchmark nuclei: ^{49}K, ^{38}Ca, ^{100}Cd, ^{119}Cd, ^{201}Po, and ^{233}Ra, and the weights of three models by BMA are based on $\delta^{\rm corr}$ of these four benchmark nuclei

Models	^{49}K	^{38}Ca	^{100}Cd	^{119}Cd	^{201}Po	^{233}Ra	Weight
HFB	0.017	−0.003	−0.017	0.007	0.007	−0.006	0.49
RHB	−0.015	0.010	0.008	−0.006	−0.017	0.009	0.38
Sheng	0.013	0.013	−0.014	0.010	0.018	−0.011	0.13

superior predictive accuracy for benchmark nuclei and is thus assigned higher weights. In contrast, the RHB model and semi-empirical formula are assigned lower weights owing to their lower predictive accuracies. The BMA method was applied to optimize the predictions for 102 validation nuclei. The standard deviation is 0.019 fm, which is lower than that of the individual model optimized by the CBP estimator, as shown in Table 2. Compared with the HFB model, the RHB model, and Sheng's formula individually optimized using the CBP estimator, the introduction of the BMA method improves the accuracy by 9.5%, 24.0%, and 26.9%, respectively. This demonstrates that the BMA method effectively combines the strengths of the different models, further enhancing predictive accuracy.

Analysis of the trend of variation in charge radii within isotopic chains reveals many important and interesting physical phenomena. This study combines the CBP and BMA methods to predict the $R_{\rm C}$ of the Ca and Sr isotopic chains, illustrating the capability of this approach to capture the physical effects within the isotopic chains. The calcium isotopic chain serves as a distinctive nuclear system for investigating interactions between protons and neutrons inside the nucleus [91–93]. In the stable isotope region of the Ca chain, ^{40}Ca and ^{48}Ca both exhibit a large number of protons and neutrons, and their $R_{\rm C}$ values are nearly identical. Owing to the change in the nuclear structure associated with shell closure, a kink in $R_{\rm C}$ at $N = 28$ is observed. For $20 < N < 28$, the trend of $R_{\rm C}$ follows a parabolic shape, and the odd–even staggering effect on $R_{\rm C}$ is particularly pronounced. For neutron-rich nuclei with $N > 28$, $R_{\rm C}$ exhibited a strong increase.

Figure 2a presents the predicted charge radii $\bar{R}$ (purple squares) for the Ca isotopic chain based on the combined CBP and BMA methods, along with uncertainty bands calculated from the corresponding error estimates. The experimental values $R_{\rm C}^{\rm exp}$ (gray circles) and initial results from the HFB model (blue squares) are also provided for comparison. The HFB model predicts an approximately linear relationship between $R_{\rm C}$ and the mass number, which deviates from the experimental results. After corrections using the CBP and BMA methods, the discrepancies between $\bar{R}$ and the experimental data were substantially reduced, providing an accurate description of the parabolic trend of $R_{\rm C}$ and kink at ^{48}Ca.

The experimental charge radii in Fig. 2a clearly show the shell effect and odd–even staggering. However, the odd–even staggering is diluted in the $R_{\rm C}$ predicted using the CBP estimator combined with the BMA method. This is because the calculation of the CBP estimator relies on nuclides with the same proton number Z or neutron number N, which leads to a weakening of the odd–even staggering effect. The introduction of the BMA method combines the results of the three models, further diluting the odd–even staggering effect.

In addition to Ca isotopes, the charge radii of Sr isotopes also exhibit prominent shell effects [94]. The Sr isotope chain extends from the valley of stability at ^{88}Sr, where isotopes show a spherical shape, to the strongly deformed

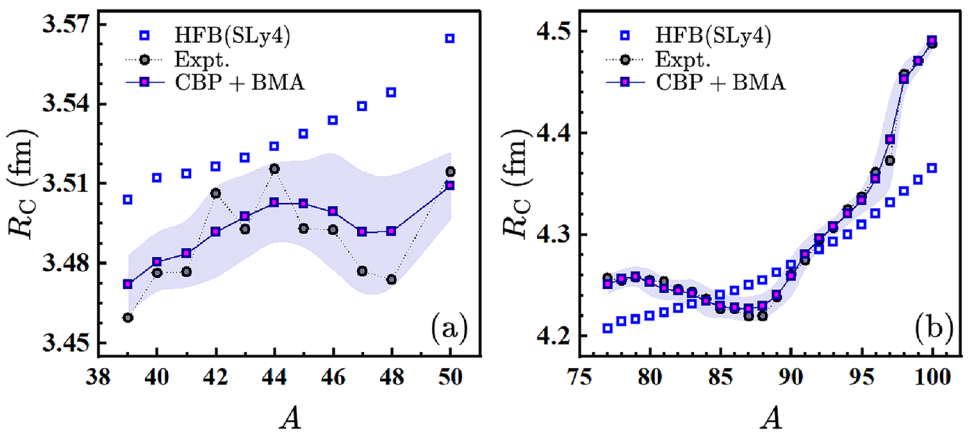

Fig. 2 **a** The theoretical and experimental charge radii $R_{\rm C}$ for Ca isotopes, with uncertainty bands included for the predictions refined by the CBP estimator. **b** Similar to **a**, but for Sr isotopes

isotopes on either side of the stability line. As the nucleus approached the neutron shell closure at $N = 50$ from the neutron-deficient side, R_C gradually decreased. At $N = 50$, it exhibited a kink, after which it began to increase. When N reached 60, a sudden increase in R_C was observed, corresponding to an experimental transition from a near-spherical shape to a strongly deformed configuration [95]. The refined predictions $\bar{R}$ of Sr isotopes obtained using the CBP estimator in conjunction with the BMA approach are shown in Fig. 2b. $\bar{R}$ was closely aligned with the experimental data, particularly for the kink of ^{88}Sr and the pronounced increase in R_C observed at ^{98}Sr.

4 Summary

This study combined the continuous Bayesian probability (CBP) estimator with Bayesian model averaging (BMA) to refine R_C predictions from the HFB, RHB, and semi-empirical formulas. In global optimization, the CBP estimator achieved an improvement of approximately 60% for all three models. In extrapolation, it demonstrates an improvement rate of approximately 45%. These results indicate that, based on sophisticated theoretical models, the CBP estimator can provide accurate predictions of R_C in the unknown regions of the nuclear chart. To enhance the predictive accuracy for nuclei near the drip line, the BMA method was subsequently employed to assign weights to each model based on their predictive performance for the benchmark nuclei. By combining the CBP estimator with the BMA method, the standard deviation is further reduced, and the physical phenomena on R_C such as shell effects in the Ca and Sr isotopic chains, are accurately captured.

The improvements achieved by the proposed method are attributed to the theoretical frameworks of the CBP estimator and the BMA method. According to the CBP estimator framework, a continuous posterior probability density function (PDF) was generated to obtain the estimated residuals for the target nucleus. The Bayesian formula captures the statistical relationships among nuclei with the same proton or neutron number, whereas the weight function accounts for the local correlations among neighboring nuclei. The theoretical models provide the overall trend of R_C, and the CBP estimator reliably refines these theoretical results through statistical techniques. Thus, the BMA method combines the strengths of different models across various regions of the nuclear chart, leading to further refinement of the results.

In summary, the CBP and BMA methods were effectively employed to predict the nuclear masses and charge radii, demonstrating considerable predictive accuracy. The methodologies developed in this work can be further extended to estimate charge radii in regions far from the β-stability line and are equally applicable to the exploration of other nuclear properties, including nuclear reactions and decay processes.

Author contributions All authors contributed to the study conception and design. Conceptualization, methodology, and writing—reviewing and editing were performed by Jian Liu. Investigation, data curation, and writing—original draft were performed by Kai-Zhong Tan and assisted by Lei Wang and Wan-Qing Gao. Part of the original data was provided by Tian-Shuai Shang and Jian Li. The manuscript was reviewed by Tian-Shuai Shang, Jian Li, and Chang Xu. All authors commented on previous versions of the manuscript. All authors read and approved the final manuscript.

Data availability The data that support the findings of this study are openly available in Science Data Bank at https://cstr.cn/31253.11.sciencedb.j00186.00763 and https://www.doi.org/10.57760/sciencedb.j00186.00763.

Declarations

Conflict of interest The authors declare that they have no conflict of interest.

References

1. M. Bender, P.H. Heenen, P.G. Reinhard, Self-consistent mean-field models for nuclear structure. Rev. Mod. Phys. **75**, 121–180 (2003). https://doi.org/10.1103/RevModPhys.75.121
2. K. Heyde, J.L. Wood, Shape coexistence in atomic nuclei. Rev. Mod. Phys. **83**, 1467–1521 (2011). https://doi.org/10.1103/RevModPhys.83.1467
3. S.J. Novario, D. Lonardoni, S. Gandolfi et al., Trends of neutron skins and radii of mirror nuclei from first principles. Phys. Rev. Lett. **130**, 032501 (2023). https://doi.org/10.1103/PhysRevLett.130.032501
4. M.Q. Ding, D.Q. Fang, Y.G. Ma, Neutron skin and its effects in heavy-ion collisions. Nucl. Sci. Tech. **35**, 211 (2024). https://doi.org/10.1007/s41365-024-01584-1
5. L. Wang, J.D. Lyu, J. Liu et al., Analysis of parity-violating electron scattering on deformed nuclei. Phys. Rev. C **109**, 064303 (2024). https://doi.org/10.1103/PhysRevC.109.064303
6. W. Geithner, T. Neff, G. Audi et al., Masses and charge radii of $^{17-22}$Ne and the two-proton-Halo candidate ^{17}Ne. Phys. Rev. Lett. **101**, 252502 (2008). https://doi.org/10.1103/PhysRevLett.101.252502
7. T. Otsuka, A. Gade, O. Sorlin et al., Evolution of shell structure in exotic nuclei. Rev. Mod. Phys. **92**, 015002 (2020). https://doi.org/10.1103/RevModPhys.92.015002
8. R.P. de Groote, J. Billowes, C.L. Binnersley et al., Measurement and microscopic description of odd-even staggering of charge radii of exotic copper isotopes. Nat. Phys. **16**, 620–624 (2020). https://doi.org/10.1038/s41567-020-0868-y
9. R. An, X. Jiang, L.G. Cao, F.S. Zhang, Odd-even staggering and shell effects of charge radii for nuclei with even Z from 36 to 38 and from 52 to 62. Phys. Rev. C **105**, 014325 (2022). https://doi.org/10.1103/PhysRevC.105.014325
10. A. Ekström, G. Hagen, T.D. Morris et al., δ isobars and nuclear saturation. Phys. Rev. C **97**, 024332 (2018). https://doi.org/10.1103/PhysRevC.97.024332

11. I. Angeli, A consistent set of nuclear rms charge radii: properties of the radius surface R(N, Z). At. Data Nucl. Data Tables **87**, 185–206 (2004). https://doi.org/10.1016/j.adt.2004.04.002
12. I. Sick, Elastic electron scattering from light nuclei. Prog. Part. Nucl. Phys. **47**, 245–318 (2001). https://doi.org/10.1016/S0146-6410(01)00156-9
13. K. Tsukada, Y. Abe, A. Enokizono et al., First observation of electron scattering from online-produced radioactive target. Phys. Rev. Lett. **131**, 092502 (2023). https://doi.org/10.1103/PhysRevLett.131.092502
14. G. Fricke, C. Bernhardt, K. Heilig et al., Nuclear ground state charge radii from electromagnetic interactions. At. Data Nucl. Data Tables **60**, 177–285 (1995). https://doi.org/10.1006/adnd.1995.1007
15. A. Krieger, K. Blaum, M.L. Bissell et al., Nuclear charge radius of ^{12}Be. Phys. Rev. Lett. **108**, 142501 (2012). https://doi.org/10.1103/PhysRevLett.108.142501
16. I. Angeli, K.P. Marinova, Table of experimental nuclear ground state charge radii: an update. At. Data Nucl. Data Tables **99**, 69–95 (2013). https://doi.org/10.1016/j.adt.2011.12.006
17. T. Li, Y. Luo, N. Wang, Compilation of recent nuclear ground state charge radius measurements and tests for models. At. Data Nucl. Data Tables **140**, 101440 (2021). https://doi.org/10.1016/j.adt.2021.101440
18. K. König, J.C. Berengut, A. Borschevsky et al., Nuclear charge radii of silicon isotopes. Phys. Rev. Lett. **132**, 162502 (2024). https://doi.org/10.1103/PhysRevLett.132.162502
19. P. Plattner, E. Wood, L. Al Ayoubi et al., Nuclear charge radius of ^{26m}Al and its implication for V_{ud} in the quark mixing matrix. Phys. Rev. Lett. **131**, 222502 (2023). https://doi.org/10.1103/PhysRevLett.131.222502
20. K. König, S. Fritzsche, G. Hagen et al., Surprising Charge-Radius Kink in the Sc Isotopes at $N = 20$. Phys. Rev. Lett. **131**, 102501 (2023). https://doi.org/10.1103/PhysRevLett.131.102501
21. J.G. Cubiss, A.N. Andreyev, A.E. Barzakh et al., Deformation versus sphericity in the ground states of the lightest gold isotopes. Phys. Rev. Lett. **131**, 202501 (2023). https://doi.org/10.1103/PhysRevLett.131.202501
22. S.Q. Zhang, J. Meng, S.G. Zhou et al., Isospin and $Z^{1/3}$- dependence of the nuclear charge radii Eur. Phys. J. A **13**, 285–289 (2002). https://doi.org/10.1007/s10050-002-8757-6
23. B. Nerlo-Pomorska, K. Pomorski, Simple formula for nuclear charge radius. Z. Phys. A **348**, 169–172 (1994). https://doi.org/10.1007/BF01291913
24. N. Wang, T. Li, Shell and isospin effects in nuclear charge radii. Phys. Rev. C **88**, 011301 (2013). https://doi.org/10.1103/PhysRevC.88.011301
25. B.H. Sun, Y. Lu, J.P. Peng et al., New charge radius relations for atomic nuclei. Phys. Rev. C **90**, 054318 (2014). https://doi.org/10.1103/PhysRevC.90.054318
26. M. Bao, Y. Lu, Y.M. Zhao, A. Arima, Predictions of nuclear charge radii. Phys. Rev. C **94**, 064315 (2016). https://doi.org/10.1103/PhysRevC.94.064315
27. M. Bao, Y.Y. Zong, Y.M. Zhao et al., Local relations of nuclear charge radii. Phys. Rev. C **102**, 014306 (2020). https://doi.org/10.1103/PhysRevC.102.014306
28. C. Ma, Y.Y. Zong, Y.M. Zhao et al., Evaluation of nuclear charge radii based on nuclear radii changes. Phys. Rev. C **104**, 014303 (2021). https://doi.org/10.1103/PhysRevC.104.014303
29. J. Barea, A. Frank, J.G. Hirsch et al., Garvey-Kelson relations and the new nuclear mass tables. Phys. Rev. C **77**, 041304 (2008). https://doi.org/10.1103/PhysRevC.77.041304
30. J. Piekarewicz, M. Centelles, X. Roca-Maza et al., Garvey-Kelson relations for nuclear charge radii. Eur. Phys. J. A **46**, 379–386 (2010). https://doi.org/10.1140/epja/i2010-11051-8
31. C. Xu, M. Bao, Improved mass relations of mirror nuclei. Nucl. Sci. Tech. **35**, 157 (2024). https://doi.org/10.1007/s41365-024-01501-6
32. P. Bano, S.P. Pattnaik, M. Centelles et al., Correlations between charge radii differences of mirror nuclei and stellar observables. Phys. Rev. C **108**, 015802 (2023). https://doi.org/10.1103/PhysRevC.108.015802
33. M.V. Stoitsov, J. Dobaczewski, W. Nazarewicz et al., Systematic study of deformed nuclei at the drip lines and beyond. Phys. Rev. C **68**, 054312 (2003). https://doi.org/10.1103/PhysRevC.68.054312
34. S. Goriely, N. Chamel, J.M. Pearson, Further explorations of Skyrme-Hartree-Fock-Bogoliubov mass formulas. XVI. Inclusion of self-energy effects in pairing. Phys. Rev. C **93**, 034337 (2016). https://doi.org/10.1103/PhysRevC.93.034337
35. R. Shou, X. Yin, C. Ma, M.Q. Lin, Y.M. Zhao, Simple corrections in theoretical models of atomic masses and nuclear charge radii. Phys. Rev. C **106**, L061304 (2022). https://doi.org/10.1103/PhysRevC.106.L061304
36. L. Wang, Q.L. Niu, J.J. Zhang et al., New extended method for ψ' scaling function of inclusive electron scattering. Sci. China Phys. Mech. Astron. **66**, 102011 (2023). https://doi.org/10.1007/s11433-023-2135-x
37. L.S. Geng, H. Toki, S. Sugimoto et al., Relativistic mean field theory for deformed nuclei with pairing correlations. Prog. Theor. Phys. **110**, 921–936 (2003). https://doi.org/10.1143/PTP.110.921
38. X.Z. Wang, Q.L. Niu, J.J. Zhang et al., Nucleon momentum distribution of ^{56}Fe from the axially deformed relativistic mean-field model with nucleon-nucleon correlations. Sci. China Phys. Mech. Astron. **64**, 292011 (2021). https://doi.org/10.1007/s11433-021-1729-5
39. Y.T. Rong, Accuracy of the mean-field theory in describing ground-state properties of light nuclei. Phys. Rev. C **108**, 054314 (2023). https://doi.org/10.1103/PhysRevC.108.054314
40. H.K. Wang, Q. Su, C. Xu et al., Influence of single-particle energy on inclusive electron scattering. J. Phys. G **50**, 095104 (2023). https://doi.org/10.1088/1361-6471/ace6c3
41. Q.L. Niu, J. Liu, Y.L. Guo et al., Effects of nucleon-nucleon short-range correlations on inclusive electron scattering. Phys. Rev. C **105**, L051602 (2022). https://doi.org/10.1103/PhysRevC.105.L051602
42. X.W. Xia, Y. Lim, P.W. Zhao et al., The limits of the nuclear landscape explored by the relativistic continuum Hartree-Bogoliubov theory. At. Data Nucl. Data Tables **121–122**, 1–215 (2018). https://doi.org/10.1016/j.adt.2017.09.001
43. P. Jiang, Z.M. Niu, Y.F. Niu, W.H. Long, Strutinsky shell correction energies in relativistic Hartree-Fock theory. Phys. Rev. C **98**, 064323 (2018). https://doi.org/10.1103/PhysRevC.98.064323
44. X.Y. Zhang, Z.M. Niu, W. Sun et al., Nuclear charge radii and shape evolution of Kr and Sr isotopes with the deformed relativistic Hartree-Bogoliubov theory in continuum. Phys. Rev. C **108**, 024310 (2023). https://doi.org/10.1103/PhysRevC.108.024310
45. K.Y. Zhang, M.K. Cheoun, Y.B. Choi et al., Nuclear mass table in deformed relativistic Hartree-Bogoliubov theory in continuum, I: Even–even nuclei. At. Data Nucl. Data Tables **144**, 101488 (2022). https://doi.org/10.1016/j.adt.2022.101488
46. P. Guo, X.J. Cao, K.M. Chen et al., Nuclear mass table in deformed relativistic Hartree-Bogoliubov theory in continuum, II: Even-Z nuclei. At. Data Nucl. Data Tables **158**, 101661 (2024). https://doi.org/10.1016/j.adt.2024.101661
47. B.N. Lu, N. Li, S. Elhatisari et al., Ab initio nuclear thermodynamics. Phys. Rev. Lett. **125**, 192502 (2020). https://doi.org/10.1103/PhysRevLett.125.192502
48. B.R. Barrett, P. Navrátil, J.P. Vary, Ab initio no core shell model. Prog. Part. Nucl. Phys. **69**, 131–181 (2013). https://doi.org/10.1016/j.ppnp.2012.10.003

49. A. Boehnlein, M. Diefenthaler, N. Sato et al., Colloquium: machine learning in nuclear physics. Rev. Mod. Phys. **94**, 031003 (2022). https://doi.org/10.1103/RevModPhys.94.031003
50. W.B. He, Q.F. Li, Y.G. Ma et al., Machine learning in nuclear physics at low and intermediate energies. Sci. China Phys. Mech. Astron. **66**, 282001 (2023). https://doi.org/10.1007/s11433-023-2116-0
51. L. Neufcourt, Y.C. Cao, W. Nazarewicz et al., Bayesian approach to model-based extrapolation of nuclear observables. Phys. Rev. C **98**, 034318 (2018). https://doi.org/10.1103/PhysRevC.98.034318
52. L. Neufcourt, Y.C. Cao, S. Giuliani et al., Beyond the proton drip line: Bayesian analysis of proton-emitting nuclei. Phys. Rev. C **101**, 014319 (2020). https://doi.org/10.1103/PhysRevC.101.014319
53. Z.M. Niu, J.Y. Fang, Y.F. Niu, Comparative study of radial basis function and Bayesian neural network approaches in nuclear mass predictions. Phys. Rev. C **100**, 054311 (2019). https://doi.org/10.1103/PhysRevC.100.054311
54. Z.M. Niu, H.Z. Liang, Nuclear mass predictions with machine learning reaching the accuracy required by *r*-process studies. Phys. Rev. C **106**, L021303 (2022). https://doi.org/10.1103/PhysRevC.106.L021303
55. X.H. Wu, P.W. Zhao, Predicting nuclear masses with the kernel ridge regression. Phys. Rev. C **101**, 051301 (2020). https://doi.org/10.1103/PhysRevC.101.051301
56. Y.H. Lu, T.S. Shang, P.X. Du et al., Nuclear mass predictions based on a convolutional neural network. Phys. Rev. C **111**, 014325 (2025). https://doi.org/10.1103/PhysRevC.111.014325
57. X.C. Ming, H.F. Zhang, R.R. Xu et al., Nuclear mass based on the multi-task learning neural network method. Nucl. Sci. Tech. **33**, 48 (2022). https://doi.org/10.1007/s41365-022-01031-z
58. Z.P. Gao, Y.J. Wang, H.L. Lü et al., Machine learning the nuclear mass. Nuc. Sci. Tech. **32**, 109 (2021). https://doi.org/10.1007/s41365-021-00956-1
59. E. Yüksel, D. Soydaner, H. Bahtiyar et al., Nuclear mass predictions using machine learning models. Phys. Rev. C **109**, 064322 (2024). https://doi.org/10.1103/PhysRevC.109.064322
60. T.S. Shang, J. Li, Z.M. Niu, Prediction of nuclear charge density distribution with feedback neural network. Nucl. Sci. Tech. **33**, 153 (2022). https://doi.org/10.1007/s41365-022-01140-9
61. T.S. Shang, H.H. Xie, J. Li et al., Global prediction of nuclear charge density distributions using a deep neural network. Phys. Rev. C **110**, 014308 (2024). https://doi.org/10.1103/PhysRevC.110.014308
62. W.F. Li, X. Y. Zhang Y. F. Niu, et al., Comparative study of neural network and model averaging methods in nuclear β-decay half-life predictions. J. Phys. G: Nucl. Part. Phys. **51**, 015103 (2023)
63. Z.S. Jin, M.S. Yan, H. Zhou et al., Bayesian optimization approach to model-based description of α decay. Phys. Rev. C **108**, 014326 (2023). https://doi.org/10.1103/PhysRevC.108.014326
64. Z.M. Niu, H.Z. Liang, B.H. Sun et al., Predictions of nuclear β -decay half-lives with machine learning and their impact on *r* -process nucleosynthesis. Phys. Rev. C **99**, 064307 (2019). https://doi.org/10.1103/PhysRevC.99.064307
65. A. Jalili, F. Pan, Y.A. Luo et al., Nuclear β-decay half-life predictions and *r*-process nucleosynthesis using machine learning models. Phys. Rev. C **111**, 034321 (2025). https://doi.org/10.1103/PhysRevC.111.034321
66. J.M. Munoz, S. Akkoyun, Z.P. Reyes et al., Predicting β-decay energy with machine learning. Phys. Rev. C **107**, 034308 (2023). https://doi.org/10.1103/PhysRevC.107.034308
67. Z.A. Wang, J.C. Pei, Optimizing multilayer Bayesian neural networks for evaluation of fission yields. Phys. Rev. C **104**, 064608 (2021). https://doi.org/10.1103/PhysRevC.104.064608
68. Z.A. Wang, J.C. Pei, Y.J. Chen et al., Bayesian approach to heterogeneous data fusion of imperfect fission yields for augmented evaluations. Phys. Rev. C **106**, L021304 (2022). https://doi.org/10.1103/PhysRevC.106.L021304
69. C.Y. Qiao, J.C. Pei, Z.A. Wang et al., Bayesian evaluation of charge yields of fission fragments of ^{239}U. Phys. Rev. C **103**, 034621 (2021). https://doi.org/10.1103/PhysRevC.103.034621
70. S. Akkoyun, T. Bayram, S.O. Kara et al., An artificial neural network application on nuclear charge radii. J. Phys. G: Nucl. Part. Phys. **40**, 055106 (2013). https://doi.org/10.1088/0954-3899/40/5/055106
71. R. Utama, W.C. Chen, J. Piekarewicz, Nuclear charge radii: density functional theory meets Bayesian neural networks. J. Phys. G: Nucl. Part. Phys. **43**, 114002 (2016). https://doi.org/10.1088/0954-3899/43/11/114002
72. X.X. Dong, R. An, J.X. Lu et al., Novel Bayesian neural network based approach for nuclear charge radii. Phys. Rev. C **105**, 014308 (2022). https://doi.org/10.1103/PhysRevC.105.014308
73. X.X. Dong, R. An, J.X. Lu et al., Nuclear charge radii in Bayesian neural networks revisited. Phys. Lett. B **838**, 137726 (2023). https://doi.org/10.1016/j.physletb.2023.137726
74. X. Zhang, H. He, G. Qu et al., Investigation of the difference in charge radii of mirror pairs with deep Bayesian neural networks. Phys. Rev. C **110**, 014316 (2024). https://doi.org/10.1103/PhysRevC.110.014316
75. Y.F. Ma, C. Su, J. Liu et al., Predictions of nuclear charge radii and physical interpretations based on the Naive Bayesian probability classifier. Phys. Rev. C **101**, 014304 (2020). https://doi.org/10.1103/PhysRevC.101.014304
76. Y.F. Liu, C. Su, J. Liu et al., Improved Naive Bayesian probability classifier in predictions of nuclear mass. Phys. Rev. C **104**, 014315 (2021). https://doi.org/10.1103/PhysRevC.104.014315
77. J.Z. Xie, K.P. Wang, C. Wang et al., Novel Bayesian probability method in predictions of nuclear masses. Phys. Rev. C **109**, 064317 (2024). https://doi.org/10.1103/PhysRevC.109.064317
78. Y. Saito, I. Dillmann, R. Krücken et al., Uncertainty quantification of mass models using ensemble Bayesian model averaging. Phys. Rev. C **109**, 054301 (2024). https://doi.org/10.1103/PhysRevC.109.054301
79. L. Neufcourt, Y. Cao, W. Nazarewicz et al., Neutron drip line in the Ca region from Bayesian model averaging. Phys. Rev. Lett. **122**, 062502 (2019). https://doi.org/10.1103/PhysRevLett.122.062502
80. Y. Saito, I. Dillmann, R. Krücken et al., Uncertainty quantification of mass models using ensemble Bayesian model averaging. Phys. Rev. C **109**, 054301 (2024). https://doi.org/10.1103/PhysRevC.109.054301
81. D.M. Rossi, K. Minamisono, H.B. Asberry et al., Charge radii of neutron-deficient ^{36}K and ^{37}K. Phys. Rev. C **92**, 014305 (2015). https://doi.org/10.1103/PhysRevC.92.014305
82. A.J. Miller, K. Minamisono, A. Klose et al., Proton superfluidity and charge radii in proton-rich calcium isotopes. Nat. Phys. **15**, 432–436 (2019). https://doi.org/10.1038/s41567-019-0416-9
83. M. Hammen, W. Nörtershäuser, D.L. Balabanski et al., From calcium to cadmium: testing the pairing functional through charge radii measurements of $^{100-130}$Cd. Phys. Rev. Lett. **121**, 102501 (2018). https://doi.org/10.1103/PhysRevLett.121.102501
84. M.D. Seliverstov, T.E. Cocolios, W. Dexters et al., Charge radii of odd-A Po isotopes. Phys. Lett. B **719**, 362–366 (2013). https://doi.org/10.1016/j.physletb.2013.01.043
85. K.M. Lynch, S.G. Wilkins, J. Billowes et al., g, Laser-spectroscopy studies of the nuclear structure of neutron-rich radium. Phys. Rev. C **97**, 024309 (2018). https://doi.org/10.1103/PhysRevC.97.024309

86. X.Y. Zhang, W.F. Li, J.Y. Fang et al., Nuclear mass predictions with the naive Bayesian model averaging method. Nucl. Phys. A **1043**, 122820 (2024). https://doi.org/10.1016/j.nuclphysa.2024.122820
87. P.W. Zhao, Z.P. Li, J.M. Yao et al., New parametrization for the nuclear covariant energy density functional with a point-coupling interaction. Phys. Rev. C **82**, 054319 (2010). https://doi.org/10.1103/PhysRevC.82.054319
88. Z.Q. Sheng, G.G. Fan, J.F. Qian et al., An effective formula for nuclear charge radii. Eur. Phys. J. A **51**, 40 (2015). https://doi.org/10.1140/epja/i2015-15040-1
89. H.H. Xie, J. Li, L.G. Jiao et al., Finite-nuclear-size effect in hydrogenlike ions with relativistic nuclear structure. Phys. Rev. A **107**, 042807 (2023). https://doi.org/10.1103/PhysRevA.107.042807
90. H.H. Xie, J. Li, Impact of intrinsic electromagnetic structure on the nuclear charge radius in relativistic density functional theory. Phys. Rev. C **110**, 064319 (2024). https://doi.org/10.1103/PhysRevC.110.064319
91. R.F. Garcia Ruiz, M.L. Bissell, K. Blaum et al., Unexpectedly large charge radii of neutron-rich calcium isotopes. Nat. Phys. **12**, 594–598 (2016). https://doi.org/10.1038/nphys3645
92. G. Co', M. Anguiano, A.M. Lallena, Charge radii of Ca isotopes and correlations. Phys. Rev. C **105**, 034320 (2022). https://doi.org/10.1103/PhysRevC.105.034320
93. T. Inakura, N. Hinohara, H. Nakada, Radial and orbital decomposition of charge radii of Ca nuclei: Comparative study of Skyrme and Fayans functionals. Phys. Rev. C **110**, 054315 (2024). https://doi.org/10.1103/PhysRevC.110.054315
94. R.E. Silverans, P. Lievens, L. Vermeeren et al., Nuclear charge radii of $^{78-100}$Sr by nonoptical detection in fast-beam laser spectroscopy. Phys. Rev. Lett. **60**, 2607–2610 (1988). https://doi.org/10.1103/PhysRevLett.60.2607
95. X.Y. Zhang, Z.M. Niu, W. Sun et al., Nuclear charge radii and shape evolution of Kr and Sr isotopes with the deformed relativistic Hartree-Bogoliubov theory in continuum. Phys. Rev. C **108**, 024310 (2023). https://doi.org/10.1103/PhysRevC.108.024310